



Vertical Air Motion Retrievals in Deep Convective Clouds using the ARM Scanning Radar Network in Oklahoma during MC3E

Kirk W. North¹, Pavlos Kollias^{1,2}, Scott E. Giangrande³, Scott M. Collis⁴, and Corey K. Potvin⁵

¹Department of Atmospheric and Oceanic Sciences, McGill University, Montreal, Quebec

²School of Marine and Atmospheric Sciences, Stony Brook University, Stony Brook, New York

³Atmospheric Sciences Division, Brookhaven National Laboratory, Upton, New York

⁴Environmental Science Division, Argonne National Laboratory, Lemont, Illinois

⁵Cooperative Institute for Mesoscale Meteorological Studies, and NOAA/OAR/National Severe Storms Laboratory, and School of Meteorology, University of Oklahoma, Norman, Oklahoma

Correspondence to: Kirk W. North (kirk.north@mail.mcgill.ca)

Abstract. The U.S. Department of Energy (DOE) Atmospheric Radiation Measurement (ARM) program's Southern Great Plains (SGP) site includes a heterogeneous distributed scanning Doppler radar network suitable for collecting coordinated Doppler velocity measurements in deep convective clouds. The surrounding National Weather Service (NWS) Next Generation Weather Surveillance Radar 1988 Doppler (NEXRAD WSR-88D) further supplements this network. Radar velocity measurements are assimilated in a three-dimensional variational (3DVAR) algorithm that retrieves horizontal and vertical air motions over a large analysis domain (100 km × 100 km) at storm-scale resolutions (250 m). For the first time, direct evaluation of retrieved vertical velocities with those from collocated 915-MHz radar wind profilers is performed. Mean absolute and root-mean-square differences between the two methods are on the order of 1 m s⁻¹ and 2 m s⁻¹, respectively. Moderate time-height correlations on the order of 0.5 are also shown to exist between the two methods. An empirical sensitivity analysis is done to determine a range of 3DVAR constraint weights that adequately satisfy both velocity observations and anelastic mass continuity. It is shown that the vertical velocity spread over this range is on the order of 1 m s⁻¹. A similar sensitivity analysis reveals that iterative multi-Doppler techniques have difficulty satisfying velocity observations and mass continuity simultaneously. These results provide a form of assurance in the use of 3DVAR retrieved vertical velocities for evaluating numerical simulations of deep convective clouds.

1 Introduction

The representation of deep convection at cloud resolving and global circulation model scales (CRMs and GCMs) remains a serious challenge (Lin et al., 2006; Jakob, 2010). Part of the challenge can be attributed to the lack of comprehensive observations of dynamics and microphysics in these vigorous cloud systems (Ferrier, 1994; Milbrandt and Yau, 2005; Mrowiec et al., 2012). In particular, cloud dynamical insights may provide necessary guidance for improving these simulations to storm scales and act as a basis for improving convective parameterizations at GCM scales (Lang et al., 2007; Wu et al., 2009; Nicol et al., 2015).



Despite the importance of vertical velocity measurements in deep convection, such measurements are not easy to acquire. Aircraft penetration of convective clouds offer the most direct method to measure these vertical air motions (Lenschow, 1976), however, practical hazards and operational costs have resulted in a valuable but limited dataset (e.g., Byers and Braham, 1948; LeMone and Zipser, 1980; Donner et al., 2001). Profiling Doppler radars have a vertical velocity retrieval uncertainty on the
5 order of $1\text{--}2\text{ m s}^{-1}$ in convective clouds, thus offer a viable substitute for in situ aircraft measurements (Jorgensen and LeMone, 1989; Cifelli and Rutledge, 1994; May and Rajopadhyaya, 1999; Williams, 2012; Heymsfield et al., 2010; Giangrande et al., 2013a; Kumar et al., 2015). Furthermore, profiling radars provide a high degree of detail of convective clouds in both time and height, and can sample even the most intense convective cores. However, profiling radars have a limited use in direct model evaluation due to their narrow view of these large, three-dimensional systems.

10 Scanning Doppler radars and the use of multi-Doppler retrieval techniques may help overcome known in situ aircraft and profiling radar sampling limitations. In addition to improved statistics of deep convection, this measurement approach offers the ability to document the three-dimensional structure of updrafts and downdrafts. However, the use of multi-Doppler retrieval techniques is not straightforward. First, the number of radars in the network and their respective locations has a direct impact on the retrieval quality. Second, distributed Doppler radar networks, including mobile radar deployments, are not widely available
15 or standardized. Operational radar networks tend to provide inadequate coverage throughout the depth of deep convective clouds, particularly at cloud top, necessary to properly constrain vertical velocity retrievals. Third, several multi-Doppler retrieval techniques have been proposed. The various techniques can be categorized as either iterative or simultaneous based on their treatment of mass continuity.

Iterative techniques solve the integral mass continuity equation throughout the column, contingent on known vertical velocity
20 boundary conditions at the bottom level (e.g., upwards integration) and/or top level (e.g., downwards integration) (e.g., O'Brien, 1970; Ray et al., 1980; Protat and Zawadzki, 1999). This first requires an estimate of horizontal wind divergence at each level made in a previous step, hence the non-simultaneity of iterative techniques (Dowell and Shapiro, 2003; Potvin et al., 2012a). By their nature, iterative techniques propagate information in one direction, thus errors in horizontal wind divergence accumulate throughout the column, which in turn leads to larger errors in vertical velocity (e.g., Ray et al., 1980).

25 Simultaneous techniques treat mass continuity similar to other analysis constraints by inserting it directly into the cost function. This avoids accumulation of errors throughout the column since mass continuity is analyzed everywhere simultaneously. Moreover, these techniques are known to mitigate retrieval instabilities in poorly constrained regions like the dual-Doppler radar baseline (Bousquet and Chong, 1998; Dowell and Shapiro, 2003). Since simultaneous techniques are by definition 3DVAR techniques, we will refer to them as such throughout the remainder of this study.

30 Several studies have investigated multi-Doppler wind retrieval uncertainties by identifying or utilizing (i) importance of Doppler radar measurement errors and beam geometry (e.g., Doviak et al., 1976; Nelson and Brown, 1987; Matejka and Bartels, 1998) (ii) influence of radar data objective analysis (e.g., Clark et al., 1980; Gal-Chen, 1982; Testud and Chong, 1983; Chong et al., 1983; Given and Ray, 1994; Majcen et al., 2008; Shapiro et al., 2010; Collis et al., 2010) and (iii) observing system simulation experiments (OSSEs) (e.g., Fanyou and Jietai, 1994; Gao et al., 1999; Liou and Chang, 2009; Potvin et al.,



2012b; Potvin and Wicker, 2012). However, few studies have explored practical retrieval performance to other independent air motion estimates from aircraft or ground-based profiling radars (e.g., Collis et al., 2013; Newsom et al., 2014)

While 3DVAR wind retrievals have been studied using OSSEs, an implementation, verification and sensitivity analysis on actual datasets is noticeably missing. The ARM SGP site in Oklahoma provides an excellent opportunity to investigate the benefits and relevant issues associated with multi-Doppler wind retrievals (Mather and Voyles, 2012). The SGP site was recently upgraded to include the installation of a distributed scanning Doppler radar network. The wind retrievals presented in this study were derived from scanning radar data collected during the Midlatitude Continental Convective Clouds Experiment (MC3E), a joint field campaign between the DOE ARM program and the National Aeronautics and Space Administration (NASA) Global Precipitation Measurement (GPM) mission Ground Validation (GV) program (Jensen et al., 2015a). This campaign also featured the deployment of four radar wind profilers, each operating in a novel deep convective mode (Tridon et al., 2013; Giangrande et al., 2013a). The four radar wind profilers were optimally placed within the scanning radar network to provide independent validation for the multi-Doppler vertical air motion retrievals.

The remainder of this paper is organized as follows. A description of the dataset and radar data processing is presented in Section 2. Section 3 provides the background for 3DVAR wind retrievals from multiple scanning Doppler radars. Retrieval sensitivity and a method for producing physically sound wind fields is discussed in Section 4. Section 5 presents 3DVAR wind retrieval results in the context of how they compare with those from independent collocated radar wind profilers as well as with an iterative upwards integration method. Section 7 is reserved for summary and concluding remarks.

2 Dataset and radar processing

The MC3E took place during April-June 2011 in northern Oklahoma and surrounding states. A total of five events from MC3E were analyzed for this study and are listed in Table 1. These events represent a variety of warm season convection over Oklahoma, including nocturnal elevated convection (25 April 2011), widespread stratiform precipitation with embedded convection (11 May 2011), mesoscale convective system (MCS) and associated squall line (20 May 2011), and isolated severe supercell thunderstorms (23-24 May 2011). The approximate time frame defining each event reflects profiling radar observations recorded at the SGP Central Facility (CF).

2.1 ARM radar network

The ARM SGP site features a network of scanning Doppler and dual-polarization radars capable of providing coordinated coverage of cloud systems over a large domain. The locations of scanning and profiling radars around the SGP CF during MC3E are shown in Fig. 1. The radar facility includes a 6.3-GHz C-band scanning ARM precipitation radar (CSAPR) and three 9.4-GHz X-band scanning ARM precipitation radars (XSAPRs). During the MC3E, a specific deep convection volume coverage pattern (VCP) was implemented in an attempt to provide dense coverage throughout the depth of typical warm season Oklahoma convection. The technical specifications of the ARM scanning radars are listed in Table 2.



Data were calibrated and processed according to several standard methods in the literature, including a conventional dual-polarization reflectivity correction for attenuation in rain appropriate for the ARM C-band radar (Bringi and Chandrasekar, 2001; Giangrande et al., 2013b, 2014; Helmus and Collis, 2016). Aliased radial velocity measurements were corrected using the four-dimensional technique described in James and Houze (2001). Similar to Collis et al. (2013), this technique was applied iteratively using multiple wind profiles from the MC3E radiosonde network to produce robust results (e.g., Jensen et al., 2015b). Finally, each radar volume was manually inspected to check for conspicuous errors and artifacts.

Following these standard procedures, radar data were mapped to a common Cartesian analysis domain. The domain for this study covers 100 km x 100 km x 10 km in meridional, zonal, and vertical extent, respectively, with 250 m grid spacing in each dimension. The horizontal area covered by the grid approximately encloses all available XSAPR coverage as shown in Fig. 1, with the SGP CF located at the origin. Since the surface elevation of the analysis domain varies less than 30 m over its entire extent, this study neglects nuances associated with complex terrain (e.g., Chong and Cosma, 2000; Liou et al., 2011). Radar data are mapped using a two-pass isotropic Barnes distance-dependent weight with a constant smoothing parameter $\kappa = 2 \text{ km}^2$ and convergence parameter $\gamma = 0.5$ (e.g., Trapp and Doswell, 2000; Majcen et al., 2008),

$$W_{i,q}(d) = \exp\left(\frac{-d_{i,q}^2}{\kappa\gamma^{p-1}}\right) \quad \forall \quad i = 1, \dots, n \quad \text{and} \quad q = 1, \dots, Q \quad (1)$$

Here $W_{i,q}$ is the weight for grid point i and radar gate q separated by distance d for pass $p = 1$ or 2. The cutoff distance defining the Q closest radar gates is the distance where the weight effectively vanishes, which is $d \approx 4 \text{ km}$. Several choices for weighting functions and their free parameters are found throughout the literature (e.g., Cressman, 1959; Barnes, 1964; Pauley and Wu, 1990; Askelson et al., 2000, 2005; Askelson and Straka, 2005; Trapp and Doswell, 2000), however the weighting function used in this study is desirable for the preservation of phase and amplitude information of the input radar data, as well as its relative insensitivity to the spatial characteristics of the input data (Trapp and Doswell, 2000).

Four 915-MHz UHF-band ARM zenith-pointing radar wind profilers (UAZR) were placed within the scanning radar network and their locations are also shown in Fig. 1. The technical details of the radar wind profilers running in a novel convection mode during MC3E are also given in Table 2. Vertical air motion retrievals from the wind profilers follow the method outlined by Giangrande et al. (2013a) and are assumed accurate to within $1\text{-}2 \text{ m s}^{-1}$ in deep convective drafts. An example of UAZR observations of convective clouds observed on 25 Apr 2011 and the corresponding vertical air motion retrieval are shown in Fig. 2. The scales of motion resolved by the UAZR are inherently different than that of the scanning radars, requiring the UAZR data to be filtered in time-height before any comparison with scanning radar retrievals can be made (see Section 5).

2.2 NEXRAD WSR-88D network

The NEXRAD WSR-88D S-band radar network surrounding the SGP site provides additional coverage and robust reflectivity measurements for each event listed in Table 1. This is especially true for 11 May 2011, where CSAPR-I7 was nonoperational yet WSR-88D reflectivity measurements were available and less susceptible to attenuation in rain than the XSAPRs.



The closest WSR-88D site to the SGP CF is Vance Air Force Base (KVNIX), located approximately 56 km west of the CF (see Figure 1). This relatively large distance, coupled with the 0.5 deg base elevation scan of KVNIX, ensures that its transmitted pulses are already 1 km above the surface directly over the CF. Figure 3 shows the nearest neighbour distance between radar gates and grid points for the 20 km x 20 km surrounding the CF assuming standard atmospheric refraction and Earth curvature (e.g., Doviak and Zrnić, 1993). The circular features seen in most cross sections are a result of discrete elevation scans. Between the surface and 2 km AGL the ARM radars have enhanced coverage compared to KVNIX. In particular, the ARM radars provide coverage that is ideal for characterizing the planetary boundary layer (PBL) since nearest neighbours are typically less than 150 m away from each other within this layer. At heights above approximately 2 km AGL, KVNIX becomes increasingly valuable, especially for grid points close to and directly above the ARM radars. The dark red shades ($d \geq 2$ km) seen in the XSAPR panels of Fig. 3 highlight the radar cone of silence, a measurement gap due to no elevation scans past 50 deg (see Table 2).

3 3DVAR wind retrieval methodology

Results presented in this study capitalize on the physical constraints of radial velocity observations, anelastic mass continuity, surface impermeability, background wind field, and spatial continuity. Assuming $\mathbf{u} = [u_1, \dots, u_n]$, $\mathbf{v} = [v_1, \dots, v_n]$, and $\mathbf{w} = [w_1, \dots, w_n]$ are the eastward, northward, and vertical wind components respectively, we have the cost function

$$J(\mathbf{u}, \mathbf{v}, \mathbf{w}) = J_o + J_c + J_p + J_b + J_s \quad (2)$$

The optimal wind field solution is at the (global) minimum of J which implies the gradient of J with respect to \mathbf{u} , \mathbf{v} , and \mathbf{w} vanishes. For applications requiring large-scale (e.g., 1×10^6 variables) nonlinear cost functional minimization, it is often necessary to use an iterative conjugate-gradient algorithm (Navon and Legler, 1987). In Gao et al. (1999), where a similar cost function and conjugate-gradient minimization algorithm were used, \mathbf{u} and \mathbf{v} were found to be well recovered within the first 50 minimization iterations, however \mathbf{w} lacked both coherency and strength until 200+ iterations. We use these values as a reference point for the minimum number of iterations required to minimize Eq. (2).

3.1 Radial velocity observations: J_o

With radial velocity observations \tilde{v}_r defined on the same n -point grid there is no need for an observation operator found in general 3DVAR schemes, and the observation constraint in Eq. (2) is instead given by

$$J_o = \frac{1}{2} \sum_{l=1}^m \left[(\mathbf{v}_r - \tilde{v}_r)^T \mathbf{\Lambda}_o (\mathbf{v}_r - \tilde{v}_r) \right] \quad (3)$$

The sum is over the m radars used in the retrieval. $\mathbf{\Lambda}_o$ is an $n \times n$ matrix analogous to the inverse observation error covariance matrix in general 3DVAR schemes with two assumptions. The first is observation errors are uncorrelated meaning $\mathbf{\Lambda}_o$ is a



diagonal matrix (this assumption extends to all other constraints as well). The second is that radial velocity observations are weighted according to maximum value of Eq. (1) during first pass. This naturally gives more weight to CSAPR and XSAPR observations within the PBL, and effectively ignores mapped observations propagated into sampling gaps such as the cone of silence. Elements of retrieved radial velocity v_r are

$$v_{r_i} = (u_i \sin \phi_i + v_i \cos \phi_i) \cos \theta_i + (w_i - w_{t_i}) \sin \theta_i \quad \forall i = 1, \dots, n \quad (4)$$

where ϕ and θ are radar azimuth and elevation pointing directions, respectively, and w_t is the bulk hydrometeor fall speed parameterized using radar reflectivity, temperature, and air density (Caya, 2001). Retrieved wind fields have been shown to be quite insensitive to the choice of fall speed parameterization (e.g., Potvin et al., 2012b).

Radial velocity observations collected from two or more radars sampling the same convective cloud system are used in Eq. (3). The radial velocity observations are assumed to be closely matched in time. We required that (a) both KVN_X and CSAPR-I7 be available (except 11 May 2011) and initiate a volume scan two minutes or less apart, and (b) any complementary XSAPR input initiate from a volume scan two minutes or less from either KVN_X or CSAPR-I7. These criteria ignore the issues associated with the advection and evolution of the cloud system (e.g., Gal-Chen, 1982; Shapiro et al., 2009).

3.2 Anelastic mass continuity: J_c

Anelastic mass continuity is known to be an adequate assumption in deep moist convection (e.g., Ogura and Phillips, 1962; Lipps, 1990). The general form of the mass continuity constraint is given by

$$J_c = \frac{1}{2} L^2 \mathbf{D}^T \mathbf{\Lambda}_c \mathbf{D} \quad (5)$$

where elements of \mathbf{D} are the anelastic mass continuity term,

$$D_i = \frac{w_i}{\rho_i} \frac{\partial \rho_i}{\partial z} + \frac{\partial u_i}{\partial x} + \frac{\partial v_i}{\partial y} + \frac{\partial w_i}{\partial z} \quad \forall i = 1, \dots, n \quad (6)$$

and all vanish if anelastic mass continuity is perfectly satisfied. L is a length scale inserted to unify the dimensions and magnitude of J_c with J_o (e.g., Legler and Navon, 1991; Bousquet and Chong, 1998; Shapiro et al., 2009). For this study we set $L = 250$ m, which is the grid spacing. In Eq. (6) ρ is air density derived from the MC3E radiosonde profiles.

Note that for iterative techniques, the vertical extent of the analysis domain controls the possible integration directions. If cloud tops are not adequately contained within the domain, a top boundary condition becomes impossible to define, making downwards integration impractical. For warm season convective clouds in Oklahoma, a domain extending upwards of 15 km AGL may be necessary in order to use downwards integration, however these heights are poorly sampled by the scanning radar network and therefore poorly constrained by observations (see Fig. 3). Furthermore, (Collis et al., 2010) showed that radar mapping artifacts aloft where radar coverage is poor leads to minimum vertical velocity errors on the order of 2 m s^{-1} at these heights. This is the primary reason for capping our analysis domain at 10 km AGL.



3.3 Surface impermeability: J_p

Surface impermeability dictates that w must vanish at the surface so we write

$$J_p = \frac{1}{2} \mathbf{w}^T \Lambda_p \mathbf{w} \quad (7)$$

It is treated as a pseudo strong constraint by heavily weighting its impact on surface grid points; non-surface grid points should not be influenced and their weights in Λ_p are set to zero.

3.4 Background wind field: J_b

Including a background constraint helps promote a wind field solution in data-sparse regions based on additional observations. The background horizontal wind components u_b and v_b are typically those from radiosonde profiles. Since vertical velocity information is unavailable from these sensors, the background constraint is written as

$$J_b = \frac{1}{2} \left[(\mathbf{u} - \mathbf{u}_b)^T \Lambda_b (\mathbf{u} - \mathbf{u}_b) + (\mathbf{v} - \mathbf{v}_b)^T \Lambda_b (\mathbf{v} - \mathbf{v}_b) \right] \quad (8)$$

Since u_b and v_b are assumed to be free of systematic errors, they are given the same weight Λ_b .

3.5 Spatial continuity: J_s

The spatial continuity constraint is essentially a low-pass filter designed to dampen high frequency perturbations in the wind retrieval. Similar to Gao et al. (1999), we define this constraint as,

$$J_s = \frac{1}{2} L^4 \left[(\nabla^2 \mathbf{u})^T \Lambda_{su} \nabla^2 \mathbf{u} + (\nabla^2 \mathbf{v})^T \Lambda_{sv} \nabla^2 \mathbf{v} + (\nabla^2 \mathbf{w})^T \Lambda_{sw} \nabla^2 \mathbf{w} \right] \quad (9)$$

In addition to reducing *noise*, Eq. (9) is able to extrapolate a wind field solution into data-sparse or poorly constrained regions. For instance, it may encourage usable solutions along the dual-Doppler baseline or add retrieval value to regions in close proximity to or directly above a radar (Bousquet and Chong, 1998).

4 Empirical wind retrieval sensitivity analysis

Typically the constraint weight matrices found in Eq. (3)-(9) are treated as adjustable parameters, controlling the degree to which each constraint influences the final solution. In essence, the values prescribed to each weight are often determined through trial and error (e.g., Gao et al., 1999). Fundamentally, there exists a range of values for each weight that produces a physically sound wind field. A thorough sensitivity analysis could be used to determine this parameter space, but this is often ignored because studies typically consider theoretical wind retrieval performance by comparing it to a known *truth* field



(e.g., model output in an OSSE). The weights that minimize the residual error between the retrieved and truth wind fields are then adopted (e.g., Gao et al., 1999; Potvin et al., 2012a). For applications involving real radar datasets where no truth field is available, one must consider (i) determining the parameter space which produces physically sound wind fields (ii) characterizing the solution spread within the parameter space determined by (i).

5 This section addresses these two points through an extensive sensitivity analysis within the experimental domain indicated by the dashed blue box in Figure 1. This domain has the same 250 m grid spacing and vertical extent as the larger domain, but covers a smaller horizontal area of 20 km x 20 km. Utilizing a smaller domain for the sensitivity analysis reduces processing time and allows for the isolation of specific cloud type regimes (e.g., convective versus stratiform). Since convective air motion retrievals are the primary interest of this study, the sensitivity analysis was done during a time when intense convection filled
 10 the experimental domain on 23 May 2011, using scanning radar observations valid between 2236-2243 UTC.

Point (i) is addressed by answering the following two questions. The first is *how well does the wind retrieval satisfy radial velocity observations?* The second is *how well does the wind retrieval satisfy anelastic mass continuity?* The second question is particularly important in the context of numerical modeling and convective parameterizations.

The wind retrieval is said to satisfy the radial velocity observations of one or more radars if the root-mean-square difference
 15 (RMSD) between the two is within the uncertainty estimate of the observations themselves. Since it is impractical to account for all sources of error inherent in mapped radial velocity observations, we establish a range of uncertainty and require the RMSD to be within this range. Radial velocity measurement error in regions of low signal-to-noise ratio and large Doppler spectrum width can be as high as 0.5 m s^{-1} . The additional uncertainty introduced when mapping irregular radial velocity data to a regular grid is estimated to be on the order of 1 m s^{-1} . Therefore, we consider the wind field to satisfy radial velocity
 20 observations if it produces a RMSD with one or more radars within $0.5\text{-}1.5 \text{ m s}^{-1}$, computed over the entire analysis domain.

To determine the degree to which the wind field satisfies anelastic mass continuity, we define the normalized mass continuity residual as

$$\text{NMCR}_i = D_i^2 \left[\left(\frac{w_i}{\rho_i} \frac{\partial \rho_i}{\partial z} \right)^2 + \left(\frac{\partial u_i}{\partial x} \right)^2 + \left(\frac{\partial v_i}{\partial y} \right)^2 + \left(\frac{\partial w_i}{\partial z} \right)^2 \right]^{-1} \quad \forall i = 1, \dots, n \quad (10)$$

where D_i is given by Eq. (6). As NMCR approaches zero, anelastic mass continuity becomes perfectly satisfied. However, this
 25 is not necessarily desirable since it is still an underlying assumption. Therefore, we propose a range for NMCR, averaged over the entire analysis domain, between 1-10%, whereby anelastic mass continuity is said to be adequately satisfied.

The response of CSAPR-I7 \tilde{v}_r RMSD and NMCR to perturbing multiple \tilde{v}_r constraint weights is analyzed, the results of which are shown in Fig. 4. The sensitivity of these two metrics to continuity-background weights is shown in Fig. 4a-b. What is immediately evident in Fig. 4a is the strong dependence of \tilde{v}_r RMSD on Λ_b , with little to no dependence on Λ_c . Even
 30 with only a factor of two increase in Λ_b , the wind retrieval diverges substantially from the radial velocity observations and converges towards the background wind field. As $\Lambda_b \rightarrow 0.5$, CSAPR-I7 \tilde{v}_r RMSD approaches the specified upper limit of 1.5 m s^{-1} . This is important to note since proponents of 3DVAR methods have reported the relative insensitivity of retrievals to minor changes (e.g., not orders of magnitude) in constraint weights (e.g., Gao et al., 1999; Potvin et al., 2012a). However,



in Fig. 4b, Λ_B has a decreased effect on the degree to which the wind retrieval satisfies mass continuity. As expected, this is primarily controlled by Λ_c , not only within the continuity-background parameter space but also in the continuity-smoothness parameter space shown in Fig. 4c-f. NMCR is particularly sensitive to Λ_c when $\Lambda_c < 250$. Outside of this range, NMCR is generally more stable with respect to Λ_c and NMCR is typically less than 20%. However, as seen in the right column of Fig. 4, in order to obtain $\text{NMCR} \leq 5\%$, Λ_c must generally be 500 or larger.

A similar sensitivity analysis was done for an iterative upwards integration technique, the results of which are shown in Fig. 5. Similar to the 3DVAR results in Fig. 4a, CSAPR-I7 \tilde{v}_r RMSD is highly dependent on Λ_B and less so on Λ_c , however for $\Lambda_c > 5$ there is a sharp increase in \tilde{v}_r RMSD up to approximately 3 m s^{-1} , well outside the 1.5 m s^{-1} upper limit. In fact, the parameter space in which \tilde{v}_r RMSD is below 1.5 m s^{-1} is very small, and when looked at together with NMCR, no continuity-background parameter space exists in which both metrics are reasonably satisfied for an iterative upwards integration technique. It is worth noting that as Λ_c is increased, NMCR appears to asymptote towards a value between 10-15%. This indicates that even in the parameter space where radial velocity observations are effectively ignored (e.g., \tilde{v}_r RMSD greater than 3 m s^{-1}), iterative upwards integration techniques still have difficulty properly satisfying mass continuity. Results were also poor for the continuity-smoothness sensitivity analysis, in particular they were more unstable, and therefore they are not shown. Therefore, we do not expect iterative upwards integration wind retrievals to necessarily satisfy mass continuity, however, radial velocity observations should be reasonably satisfied.

Unlike the continuity-background sensitivity analysis, both metrics appear highly unstable in certain regions of the continuity-smoothness parameter spaces investigated in Fig. 4c-f. For Λ_{su} and Λ_{sv} , which control the degree of smoothing of the horizontal wind components in Eq. (9), CSAPR-I7 \tilde{v}_r RMSD becomes unstable as these two weights approach values of 400 and larger. A similar phenomenon occurs for NMCR in Fig. 4d. These highly unstable regions of the parameter space are likely the result of nonlinear effects introduced by the squared second order partial derivatives defined in J_s and should be avoided altogether. For values of Λ_{su} and Λ_{sv} below approximately 100, CSAPR-I7 \tilde{v}_r RMSD is within 1.5 m s^{-1} and relatively stable. However, the parameter space in which this holds true gradually shrinks as Λ_c increases towards 1000. Mass continuity is also adequately satisfied for $\Lambda_{su} = \Lambda_{sv} < 100$ and $\Lambda_c > 250$, with NMCR typically less than 10%. Results for Λ_{sw} are similar to those of Λ_{su} and Λ_{sv} except for one aspect. Since Λ_{sw} controls the degree of smoothing of the vertical wind component in J_s , it has little influence on CSAPR-I7 \tilde{v}_r RMSD since the vertical wind component is generally not well sampled by scanning radars. This manifests itself in Fig. 4e, which shows CSAPR-I7 \tilde{v}_r RMSD to have much less dependence on Λ_{sw} compared to Λ_{su} and Λ_{sv} . A summary of the findings from this sensitivity analysis is recorded in Table 3.

4.1 Vertical velocity solution spread

Each panel in Fig. 4 contains over 2000 wind field realizations, each of which was concurrently saved. Therefore, we compute the 3DVAR vertical velocity solution spread from these thousands of realizations, allowing us to address point (ii) above. It was found that within the range of constraint weights defined in the analysis column of Table 3, the vertical velocity solution spread was relatively narrow at 1.5 m s^{-1} . This provides a form of uncertainty estimate for the 3DVAR wind retrievals presented in



this study. It follows that we expect the 3DVAR vertical velocity retrievals to be relatively stable over a large range of constraint weights, with an uncertainty estimate on the order of 1-2 m s⁻¹.

5 Evaluation with collocated profiling radars

Wind fields retrieved from scanning Doppler radars, with an emphasis on vertical air motion, have not faced critical evaluation against independent observational datasets. Collis et al. (2013) recently compared iterative dual-Doppler wind retrievals in tropical convection with those from a collocated dual-frequency wind profiler. However, because of the suboptimal location of the wind profiler near the dual-Doppler baseline, several assumptions had to be made before evaluating the two datasets.

Inherent differences between profiling and scanning radar observations restrict a direct comparison between the two datasets. The primary differences are related to temporal and spatial alignments of sampled radar volumes, beam broadening effects, and potential radar miscalibration. The 6 s temporal resolution of the UAZR dataset is considerably higher than that of the scanning radars, which return to the same location every 6-7 minutes. Furthermore, the 120 m vertical resolution of the UAZR dataset is higher than the discrete elevation sampling of the scanning radars, especially for higher elevation scans where consecutive elevations are separated by more than 5 deg. Beam width and beam broadening effects must also be taken into account. Therefore a two-dimensional time-height median filter is first applied to the UAZR dataset in order to remove high frequency, time-dependent phenomena and small-scale turbulent structures unresolvable by the scanning radars. We use a filter that is 61 time profiles in width (6 minutes) by 7 range gates (840 m) in height.

Using the time record and the fixed location of the UAZRs, the closest grid column in space and time is identified. Surrounding each identified grid column we define a radius of influence R_s set to 750 m, implemented to account for the spatiotemporal sampling differences between the two datasets, as well as the advection of the cloud system. At each grid level, the median value within R_s is used as the best estimate, and the range of values within R_s are used to estimate the variability (e.g., spatial uncertainty) of the scanning radars. Similarly, at each UAZR range (height) gate, the median value within the time window of the corresponding scanning radar data (herein the valid time) is used as the best estimate for the UAZR, and the range of UAZR values within the valid time is used to characterize its variability. Several common error statistics are used to compare the two datasets: mean bias error (MBE), mean absolute error (MAE), root-mean-square error (RMSE), Spearman's rank correlation (ρ), and the Pearson product-moment correlation (r). Difference statistics are computed subtracting UAZR from scanning radar, so a negative bias implies the scanning radar dataset underestimated the corresponding UAZR dataset.

5.1 Radar reflectivity comparisons

The comparison criteria are evaluated by comparing radar reflectivity Z_H measurements observed by UAZR-C1 with those from CSAPR-I7. These measurements are more direct, and the two radars are calibrated. The UAZR receiver is known to saturate below 1 km range in heavy precipitation (e.g., ~ 45 dBZ at 1 km range), therefore comparisons are performed above this level. Below the melting layer, the two Z_H time series are moderately correlated, with ρ and r typically above 0.8 and 0.6, respectively, and MAE below 3 dBZ. Table 4 provides a summary of each comparative statistic at three characteristic heights



for all events. The characteristic heights represent those below the melting layer (2 km AGL) and above the melting layer (6-8 km AGL). We note that the comparisons typically deteriorate within the melting layer (2.5-3.5 km AGL) due to additional wavelength-dependent scattering phenomena.

Figure 6 shows the Z_H time series of both CSAPR-I7 and UAZR-C1 at the three characteristic heights on 20 May 2011. The two datasets are visually highly correlated, with correlation coefficients typically above 0.8, MAE below 2.5 dBZ, and RMSE below 3.8 dBZ. This particular event included the formation and subsequent passage of a squall line directly over CSAPR-I7 around 1040 UTC. The large Z_H difference between CSAPR-I7 and UAZR-C1 between 1030-1100 UTC is a result of radome-induced attenuation effects on the measured CSAPR-I7 reflectivities. This highlights the need to incorporate observations from a longer-wavelength radar such as KVNK which is less susceptible to radome and path attenuation in heavy rain. To demonstrate this, KVNK Z_H is superimposed in Fig. 6 exclusively between 1000-1100 UTC to show the improvement it offers in Z_H observations of the squall line.

Overall, the Z_H comparisons shown here indicate that these two independent datasets are reasonably well matched. As a final note, the observed discrepancies between Z_H as indicated by both the MAE and RMSE values in Table 4 are arguably comparable to the limit one may be able to reliably calibrate radar systems using natural media under Oklahoma conditions (Ryzhkov et al., 2005; Giangrande and Ryzhkov, 2005).

5.2 Vertical air motion comparisons

The 25 April 2011 event was the first coordinated aircraft-ground precipitation mission during MC3E. Convective cells developed during the nighttime across northern parts of Oklahoma and along an elevated front, aided by mid to upper-level ascent associated with the passage of an upper-level trough. The convective cells were relatively shallow in depth. Figure 7a shows the time-height of vertical air motion retrievals and corresponding reflectivity from UAZR-C1. The closest available 3DVAR retrieval and its reflectivity field are shown in Fig. 7b-e. The 3DVAR retrieval used scanning radar observations recorded between 0916-0924 UTC, spanning a total of 8 minutes. The most prominent feature in both retrievals is the elevated updraft with an apparent base extending slightly below 4 km AGL, a depth of 5-6 km, and an intensity greater than 8 m s^{-1} . The local system advection speed was estimated to be 18 m s^{-1} by Giangrande et al. (2013a), with a north-northeast direction inferred by comparing successive CSAPR-I7 reflectivity displays. Therefore the time axis in Fig. 7a was reversed to better represent what the updraft retrieved by UAZR-C1 would look like in the north-south vertical cross section in Fig. 7e. The base of the updraft retrieved by UAZR-C1 is first seen at approximately 0923 UTC, which is near the end of the 3DVAR valid time window. The base of the updraft in the 3DVAR retrieval is approximately 2 km south of UAZR-C1, and with the prescribed system motion would pass over UAZR-C1 2 minutes later. This 2 minute (2 km) offset is consistent with the UAZR-C1 retrieval if we assume that the 3DVAR retrieval is valid at 0921 UTC, which is within the valid time. The two independent vertical air motion retrievals are qualitatively consistent with one another in terms of the relative location of the main updraft, its base height and depth, and its overall intensity.

A more direct time-height comparison between these two methods for the same event covering 0900-1045 UTC is provided in Fig. 8. In this case, the UAZR-C1 data has been filtered using the 61×7 time-height median filter. The elevated updraft seen



in Fig. 7 is easily identifiable in the 6 km and 8 km AGL panels between 0915-0930 UTC for both retrievals, with each showing the updraft strength to be stronger at 8 km rather than 6 km AGL. Visually the two retrievals are reasonably correlated at each height, with $r = 0.51$ and MAE less than 2 m s^{-1} at 6 km AGL (Table 5). The updraft retrieved by the 3DVAR method as seen in Fig. 7 that was offset by approximately 2 minutes (2 km) from the UAZR-C1 location is well-captured by the 3DVAR error bars between 0915-0930 UTC in Fig. 8b-c. Table 5 reports the remaining errors and correlations between the two methods for this event. At most characteristic heights, vertical velocity bias is near 0.5 m s^{-1} and absolute error is less than 2 m s^{-1} . This is negligible when considering the inherent differences between the two methods and the small percent error this would suggest between intense convective drafts (e.g., $10\text{-}20 \text{ m s}^{-1}$). The correlation coefficients are moderate at heights 6 km AGL and below (not all shown), with values of ρ and r between 0.4 and 0.6. At higher altitudes such as 8 km AGL, correlations are weaker and errors are larger, likely the result of the elevated nature of this event and thus the stronger dynamics aloft. That said, the vertical air motion time series at 8 km AGL still appears to show some skill between the two methods, with a bias less than 0.5 m s^{-1} and 3DVAR error bars indicating a better correlation than is otherwise shown at this height in Table 5.

The 20 May 2011 event was the longest lived propagating MCS sampled by the scanning radar network during MC3E. UAZR-C1 observed leading stratiform precipitation and shallow convection throughout 0600-1000 UTC, followed by deep convection between 1000-1100 UTC which ultimately produced a large region of trailing stratiform precipitation that existed over UAZR-C1 for another 4-5 hours. The most interesting feature of this event from a wind retrieval standpoint was the development of a well-organized squall line, passing over UAZR-C1 around 1040 UTC. Similar to Fig. 8, the temporal comparisons at three characteristic heights between UAZR-C1 and 3DVAR wind retrievals for this event are shown in Fig. 9, covering the 6 hours between 0700-1300 UTC. Strong upwards motion associated with the squall line surface convergence zone is immediately visible at the 2 km AGL time series in Fig. 9a for both methods. The 3DVAR vertical velocities near this time at 2 km AGL reach upwards of 13 m s^{-1} , similar to the instantaneous, unfiltered values retrieved by UAZR-C1 (not shown). The large range of vertical velocities in R_s (e.g., $\sim 8 \text{ m s}^{-1}$ at 2 km AGL) between 1015-1045 UTC are an indication of the strong dynamics associated with the squall line. Overall there is good agreement between the two methods surrounding the squall line as well as throughout the rest of the 6 hour period. Vertical velocity correlations as high as 0.7-0.8 were found at select heights between 2 km and 8 km AGL (not shown), with the entire event producing a moderate correlation of $r = 0.5$ (see Table 5). Vertical velocity errors were also relatively small, with biases approaching 0.3 m s^{-1} , absolute errors generally smaller than 1 m s^{-1} , and root mean square errors below 1.5 m s^{-1} .

The 23 May 2011 event was part of an active sequence of severe convective outbreak days over the central plains. A surface low pressure system located over the Texas panhandle and the associated surface boundaries were focal points for late afternoon convection. The environmental forcing coupled with strong daytime heating led to significant instability in addition to deep layer shear consistent with the eventual development of strong, discrete supercells. Convection captured within the analysis domain developed ahead of a surface dry line in western Oklahoma, coinciding with the passage of a shortwave trough. Supercells propagated eastward into the analysis domain by 2100 UTC, with UAZR-I9 observing intense, deep convection between 2200-2300 UTC. Near 2235 UTC, UAZR-I9 retrieved strong downdrafts reaching the surface with magnitudes larger than 8 m s^{-1} , with the core of the downdrafts increasing in height in the 8-10 minutes that followed. These results are shown



in Fig. 10a. The closest available 3DVAR retrieval, valid between 2236-2243 UTC, is shown in Fig. 10b-e. Due to the east-northeast propagation of the local cloud system, the time axis in Fig. 10a was reversed to better reflect the east-west cross section through the 3DVAR retrieval in Fig. 10d. Cloud advection speed was estimated to be 17 m s^{-1} , indicating that the total downdraft feature retrieved by UAZR-I9 between roughly 2235-2245 UTC (10 minutes) covered approximately 10 km in length. This length is consistent with the east-west length of the total downdraft feature retrieved by the 3DVAR method in Fig. 10d, which covers the zonal length roughly between $x = -6 \text{ km}$ and $x = 4 \text{ km}$. Furthermore, the behaviour of the retrieved 3DVAR downdraft is consistent with that of UAZR-I9, namely a surface bound downdraft which appears to elevate as time (displacement) increases.

6 3DVAR versus iterative upwards integration retrievals

Some of the added benefits of 3DVAR over an iterative upwards integration technique were discussed in Section 4 through an extensive sensitivity analysis. It was shown that there was a large parameter space in which 3DVAR retrievals were able to simultaneously satisfy radial velocity observations and mass continuity, with the retrieved vertical velocity relatively stable over this space. The same could not be said for the iterative upwards integration technique, which never adequately satisfied mass continuity (e.g., NMCR was never less than 10%) and radial velocity observations were, for the most part, difficult to adequately satisfy. Here we investigate what role this has on the actual wind fields retrieved by both techniques. This is accomplished by selecting the squall line event on 20 May 2011, which had substantial surface wind convergence ahead of the line that was well sampled by the scanning radar network. Strong wind convergence at or near the surface was indirectly observed around 1040 UTC by UAZR-C1 as strong upwards motion lasting close to 5 minutes (see Figure 9a). An upwards integration technique is ideal for surface-driven events since the horizontal wind divergence profile should be well defined, particularly near the lower boundary.

Figure 11 presents the wind retrievals from these two methods within the $20 \text{ km} \times 20 \text{ km}$ area surrounding the CF. Both methods retrieve similar wind convergence patterns and upwards motion at 1 km AGL, with the iterative technique retrieving a slightly stronger convergence line near the surface and therefore enhanced upwards air motion near the surface. Both methods also satisfy radial velocity observations below 2 km AGL, as shown in Fig. 11f. However, as expected, there is a large discrepancy between the two methods when it comes to satisfying mass continuity. At each analysis height in Fig. 11g, the 3DVAR retrieval is adequately satisfying mass continuity, with $\text{NMCR} < 10\%$ at each height and $\text{NMCR} = 5\%$ over the entire domain. For the iterative retrieval, NMCR never gets below 30% at any given height, and over the entire domain $\text{NMCR} = 52\%$. Differences in the vertical velocity field between both techniques becomes more pronounced with increasing height due in part to the iterative retrieval not adequately satisfying mass continuity throughout the column. At 8 km AGL, the vertical velocity fields no longer exhibit similar spatial patterns or intensities. This accumulation of differences with height is most evident in Fig. 11f. For the iterative retrieval, CSAPR-I7 \vec{v}_r RMSD quickly grows larger than 2 m s^{-1} at heights above 5 km AGL whereas the 3DVAR method is able to satisfy CSAPR-I7 radial velocity observations at almost all analysis levels. As a result, the large spread in vertical velocity differences between the two retrievals shown in Fig. 11h primarily comes from



analysis levels above 5 km AGL. Over the entire analysis domain, vertical velocity MBE, MAE, and RMSE are all significant at 1.3 m s^{-1} , 5.8 m s^{-1} , and 7.7 m s^{-1} , respectively. Conditionally sampling the two retrievals below 5 km AGL, the MBE, MAE, and RMSE decrease substantially to 0.5 m s^{-1} (38%), 2.6 m s^{-1} (45%), and 3.9 m s^{-1} (51%), respectively. Nonetheless, this still represents large differences in the wind fields retrieved by each technique.

5 7 Summary

This study addresses the utilization of the ARM SGP scanning radar network in retrieving robust air motion estimates in deep convective clouds. With the inclusion of surrounding NEXRAD WSR-88D assets, this study marks the first time X-, C-, and S-band scanning radars have been used together to pseudo simultaneously view the atmosphere from multiple different angles and retrieve the wind field over a large domain.

10 Results were broken up into three subsections. The first evaluated how well collocated column measurements of radar reflectivity from radar wind profilers could be matched with those from scanning radars. Time-height comparisons showed good visual agreement between reflectivity measurements, which was reinforced by correlations greater than 0.8 at most heights, MBE near -1.5 dB, and MAE typically less than 3 dB. A similar evaluation was done for vertical air motion retrievals, the results of which were encouraging. The spatial and temporal characteristics of 3DVAR vertical velocity retrievals were
15 generally in good agreement with those from the profiling radars. Prominent updraft and downdraft features retrieved by the UAZRs were repeatedly observed in the 3DVAR dataset. Time-height comparisons showed reasonable agreement for most events analyzed, with moderate correlations on the order of 0.5, MBE less than 0.5 m s^{-1} , MAE within 1 m s^{-1} , and RMSE generally less than 1.5 m s^{-1} . In the context of deep convective drafts, where velocities can easily exceed 15 m s^{-1} , these differences are arguably negligible. Finally, an evaluation of the wind field surrounding the 20 May 2011 squall line was
20 done. Here we investigated the underlying differences between 3DVAR and an iterative upwards integration retrieval. Below approximately 5 km AGL, the two techniques retrieved similar vertical velocity spatial patterns, including a large region of upwards motion associated with the surface convergence zone. However, the magnitudes of the vertical velocities between the two methods were considerably different, with MAE and RMSE on the order of 3 m s^{-1} and 4 m s^{-1} , respectively. These large differences were likely caused by the iterative technique inadequately satisfying mass continuity. In particular, the mean NMCR
25 was 52% for the iterative retrieval compared to 5% for the 3DVAR retrieval. Additionally, radial velocity RMSE quickly grew larger than 2 m s^{-1} above 5 km AGL for the iterative retrieval, further indicating suspect results. Overall, the iterative wind retrieval was inferior to its 3DVAR counterpart.

The ARM SGP site promises to provide a unique convective air motion dataset moving forward due to its continuous operation. Plans are currently being made for a second C-band radar to be placed due south of the SGP CF, which would
30 provide an additional constraint for these retrievals. With this in mind, we have the ability to create a large, high quality dataset of continental convective air motions over a large domain derived from radial velocity observations. This dataset would provide, at minimum, an additional observational constraint for improving current convective parameterizations used in CRMs and GCMs.



Author contributions. The contribution of Scott Giangrande through Brookhaven National Laboratory was supported by the U.S. Department of Energy under contract DE-AC02-98CH10886. The contribution of Scott Collis through Argonne National Laboratory was supported by the U.S. Department of Energy, Office of Science, Office of Biological and Environmental Research, under Contract DE-AC02-06CH11357.

Acknowledgements. Data were obtained from the Atmospheric Radiation Measurement (ARM) Program sponsored by the U.S. Department of Energy, Office of Science, Office of Biological and Environmental Research, Climate and Environmental Sciences Division. The publisher by accepting the paper for publication acknowledges that the U.S. government retains a nonexclusive, paid-up, irrevocable, worldwide license to publish or reproduce the published form of this paper, or to allow others to do so, for U.S. government purposes.



References

- Askelson, M. A. and Straka, J. M.: Response Functions for Arbitrary Weight Functions and Data Distributions. Part I: Framework for Interpreting the Response Function, *Mon. Wea. Rev.*, 133, 2117–2131, 2005.
- Askelson, M. A., Aubagnac, J.-P., and Straka, J. M.: An Adaptation of the Barnes Filter Applied to the Objective Analysis of Radar Data, *Mon. Wea. Rev.*, 128, 3050–3082, 2000.
- Askelson, M. A., Pauley, P. M., and Straka, J. M.: Response Functions for Arbitrary Weight Functions and Data Distributions. Part II: Response Function Derivation and Verification, *Mon. Wea. Rev.*, 133, 2132–2147, 2005.
- Barnes, S. L.: A Technique for Maximizing Details in Numerical Weather Map Analysis, *J. Appl. Meteor.*, 3, 396–409, 1964.
- Bousquet, O. and Chong, M.: A Multiple-Doppler Synthesis and Continuity Adjustment Technique (MUSCAT) to Recover Wind Components from Doppler Radar Measurements, *J. Atmos. Oceanic Technol.*, 15, 343–359, 1998.
- Bringi, V. N. and Chandrasekar, V.: *Polarimetric Doppler Weather Radar: Principles and Applications*, Cambridge University Press, 2001.
- Byers, H. R. and Braham, R. R.: Thunderstorm structure and circulation, *J. Meteor.*, 5, 71–86, 1948.
- Caya, A.: Assimilation of radar observations into a cloud-resolving model, Ph.d., McGill University, Montreal, Quebec, 2001.
- Chong, M. and Cosma, S.: A Formulation of the Continuity Equation of MUSCAT for either Flat or Complex Terrain, *J. Atmos. Oceanic Technol.*, 17, 1556–1565, 2000.
- Chong, M., Testud, J., and Roux, F.: Three-Dimensional Wind Field Analysis from Dual-Doppler Radar Data. Part II: Minimizing the Error due to Temporal Variation, *J. Climate Appl. Meteor.*, 22, 1216–1226, 1983.
- Cifelli, R. and Rutledge, S. A.: Vertical Motion Structure in Maritime continent mesoscale Convective Systems: Results from a 50-MHz Profiler, *J. Atmos. Sci.*, 51, 2631–2652, 1994.
- Clark, T. L., Harris, F. I., and Mohr, C. G.: Errors in Wind Fields Derived from Multiple-Doppler Radars: Random Errors and Temporal Errors Associated with Advection and Evolution, *J. Appl. Meteor.*, 19, 1273–1284, 1980.
- Collis, S., Protat, A., and Chung, K.-S.: The Effect of Radial Velocity Gridding Artifacts on Variationally Retrieved Vertical Velocities, *J. Atmos. Oceanic Technol.*, 27, 1239–1246, 2010.
- Collis, S., Protat, A., May, P. T., and Williams, C.: Statistics of Storm Updraft Velocities from TWP-ICE Including Verification with Profiling Measurements, *J. Appl. Meteor. Climatol.*, 52, 1909–1922, 2013.
- Cressman, G. P.: An operational objective analysis system, *Mon. Wea. Rev.*, 87, 367–374, 1959.
- Donner, L. J., Seman, C. J., Hemler, R. S., and Fan, S.: A Cumulus Parameterization Including Mass Fluxes, Convective Vertical Velocities, and Mesoscale Effects: Thermodynamic and Hydrological Aspects in a General Circulation Model, *J. Climate*, 14, 3444–3463, 2001.
- Doviak, R. J. and Zrić, D. S.: *Doppler Radar and Weather Observations*, Courier Corporation, 1993.
- Doviak, R. J., Ray, P. S., Strauch, R. G., and Miller, L. J.: Error Estimation in Wind Fields Derived from Dual-Doppler Radar Measurement, *J. Appl. Meteor.*, 15, 868–878, 1976.
- Dowell, D. C. and Shapiro, A.: Stability of an Iterative Dual-Doppler Wind Synthesis in Cartesian Coordinates, *J. Atmos. Oceanic Technol.*, 20, 1552–1559, 2003.
- Fanyou, K. and Jietai, M.: A Model study of three-dimensional wind field analysis from dual-doppler radar data, *Advances in Atmospheric Sciences*, 11, 162–174, 1994.
- Ferrier, B. S.: A Double-Moment Multiple-Phase Four-Class Bulk Ice Scheme. Part I: Description, *J. Atmos. Sci.*, 51, 249–280, 1994.



- Gal-Chen, T.: Errors in Fixed and Moving Frame of References: Applications for Conventional and Doppler Radar Analysis, *J. Atmos. Sci.*, 39, 2279–2300, 1982.
- Gao, J., Xue, M., Shapiro, A., and Droegeleier, K. K.: A Variational Method for the Analysis of Three-Dimensional Wind Fields from Two Doppler Radars, *Mon. Wea. Rev.*, 127, 2128–2142, 1999.
- 5 Giangrande, S. E. and Ryzhkov, A. V.: Calibration of Dual-Polarization Radar in the Presence of Partial Beam Blockage, *J. Atmos. Oceanic Technol.*, 22, 1156–1166, 2005.
- Giangrande, S. E., Collis, S., Straka, J., Protat, A., Williams, C., and Krueger, S.: A Summary of Convective-Core Vertical Velocity Properties Using ARM UHF Wind Profilers in Oklahoma, *Journal of Applied Meteorology and Climatology*, 52, 2278–2295, 2013a.
- Giangrande, S. E., McGraw, R., and Lei, L.: An Application of Linear Programming to Polarimetric Radar Differential Phase Processing, *J.*
10 *Atmos. Oceanic Technol.*, 30, 1716–1729, 2013b.
- Giangrande, S. E., Collis, S., Theisen, A. K., and Tokay, A.: Precipitation Estimation from the ARM Distributed Radar Network during the MC3E Campaign, *J. Appl. Meteor. Climatol.*, 53, 2130–2147, 2014.
- Given, T. and Ray, P. S.: Response of a Two-Dimensional Dual-Doppler Radar Wind Synthesis, *J. Atmos. Oceanic Technol.*, 11, 239–255, 1994.
- 15 Helmus, J. and Collis, S.: The Python ARM Radar Toolkit (Py-ART), a Library for Working with Weather Radar Data in the Python Programming Language, *Journal of Open Research Software*, 4, 2016.
- Heymsfield, G. M., Tian, L., Heymsfield, A. J., Li, L., and Guimond, S.: Characteristics of Deep Tropical and Subtropical Convection from Nadir-Viewing High-Altitude Airborne Doppler Radar, *J. Atmos. Sci.*, 67, 285–308, 2010.
- Jakob, C.: Accelerating Progress in Global Atmospheric Model Development through Improved Parameterizations: Challenges, Opportuni-
20 ties, and Strategies, *Bull. Amer. Meteor. Soc.*, 91, 869–875, 2010.
- James, C. N. and Houze, R. A.: A Real-Time Four-Dimensional Doppler Dealiasing Scheme, *J. Atmos. Oceanic Technol.*, 18, 1674–1683, 2001.
- Jensen, M. P., Petersen, W. A., Bansemmer, A., Bharadwaj, N., Carey, L. D., Cecil, D. J., Collis, S. M., Del Genio, A. D., Dolan, B., Gerlach, J., Giangrande, S. E., Heymsfield, A., Heymsfield, G., Kollias, P., Lang, T. J., Nesbitt, S. W., Neumann, A., Poellot, M., Rutledge, S. A.,
25 Schwaller, M., Tokay, A., Williams, C. R., Wolff, D. B., Xie, S., and Zipser, E. J.: The Midlatitude Continental Convective Clouds Experiment (MC3E), *Bull. Amer. Meteor. Soc.*, 2015a.
- Jensen, M. P., Toto, T., Troyan, D., Ciesielski, P. E., Holdridge, D., Kyrouac, J., Schatz, J., Zhang, Y., and Xie, S.: The Midlatitude Continental Convective Clouds Experiment (MC3E) sounding network: operations, processing and analysis, *Atmos. Meas. Tech.*, 8, 421–434, 2015b.
- Jorgensen, D. P. and LeMone, M. A.: Vertically Velocity Characteristics of Oceanic Convection, *J. Atmos. Sci.*, 46, 621–640, 1989.
- 30 Kumar, V. V., Jakob, C., Protat, A., Williams, C. R., and May, P. T.: Mass-Flux Characteristics of Tropical Cumulus Clouds from Wind Profiler Observations at Darwin, Australia, *J. Atmos. Sci.*, 72, 1837–1855, 2015.
- Lang, S., Tao, W.-K., Simpson, J., Cifelli, R., Rutledge, S., Olson, W., and Halverson, J.: Improving Simulations of Convective Systems from TRMM LBA: Easterly and Westerly Regimes, *J. Atmos. Sci.*, 64, 1141–1164, 2007.
- Legler, D. M. and Navon, I. M.: VARIATM - A FORTRAN Program for Objective Analysis of Pseudostress Wind Fields Using Large-scale
35 Conjugate-gradient Minimization, *Comput. Geosci.*, 17, 1–21, 1991.
- LeMone, M. A. and Zipser, E. J.: Cumulonimbus Vertical Velocity Events in GATE. Part I: Diameter, Intensity and Mass Flux, *J. Atmos. Sci.*, 37, 2444–2457, 1980.
- Lenschow, D. H.: Estimating Updraft Velocity from an Airplane Response, *Mon. Wea. Rev.*, 104, 618–627, 1976.



- Lin, J.-L., Kiladis, G. N., Mapes, B. E., Weickmann, K. M., Sperber, K. R., Lin, W., Wheeler, M. C., Schubert, S. D., Del Genio, A., Donner, L. J., Emori, S., Gueremy, J.-F., Hourdin, F., Rasch, P. J., Roeckner, E., and Scinocca, J. F.: Tropical Intraseasonal Variability in 14 IPCC AR4 Climate Models. Part I: Convective Signals, *J. Climate*, 19, 2665–2690, 2006.
- Liou, Y.-C. and Chang, Y.-J.: A Variational Multiple-Doppler Radar Three-Dimensional Wind Synthesis Method and Its Impacts on Thermodynamic Retrieval, *Mon. Wea. Rev.*, 137, 3992–4010, 2009.
- Liou, Y.-C., Chang, S.-F., and Sun, J.: An Application of the Immersed Boundary Method for Recovering the Three-Dimensional Wind Fields over Complex Terrain Using Multiple-Doppler Radar Data, *Mon. Wea. Rev.*, 140, 1603–1619, 2011.
- Lipps, F. B.: On the Anelastic Approximation for Deep Convection, *J. Atmos. Sci.*, 47, 1794–1798, 1990.
- Majcen, M., Markowski, P., Richardson, Y., Dowell, D., and Wurman, J.: Multipass Objective Analyses of Doppler Radar Data, *J. Atmos. Oceanic Technol.*, 25, 1845–1858, 2008.
- Matejka, T. and Bartels, D. L.: The Accuracy of Vertical Air Velocities from Doppler Radar Data, *Mon. Wea. Rev.*, 126, 92–117, 1998.
- Mather, J. H. and Voyles, J. W.: The Arm Climate Research Facility: A Review of Structure and Capabilities, *Bull. Amer. Meteor. Soc.*, 94, 377–392, 2012.
- May, P. T. and Rajopadhyaya, D. K.: Vertical Velocity Characteristics of Deep Convection over Darwin, Australia, *Mon. Wea. Rev.*, 127, 1056–1071, 1999.
- Milbrandt, J. A. and Yau, M. K.: A Multimoment Bulk Microphysics Parameterization. Part II: A Proposed Three-Moment Closure and Scheme Description, *J. Atmos. Sci.*, 62, 3065–3081, 2005.
- Mrowiec, A. A., Rio, C., Fridlind, A. M., Ackerman, A. S., Del Genio, A. D., Pauluis, O. M., Varble, A. C., and Fan, J.: Analysis of cloud-resolving simulations of a tropical mesoscale convective system observed during TWP-ICE: Vertical fluxes and draft properties in convective and stratiform regions, *J. Geophys. Res.*, 117, D19 201, 2012.
- Navon, I. M. and Legler, D. M.: Conjugate-Gradient Methods for Large-Scale Minimization in Meteorology, *Mon. Wea. Rev.*, 115, 1479–1502, 1987.
- Nelson, S. P. and Brown, R. A.: Error Sources and Accuracy of Vertical Velocities Computed from Multiple-Doppler Radar Measurements in Deep Convective Storms, *J. Atmos. Oceanic Technol.*, 4, 233–238, 1987.
- Newsom, R. K., Berg, L. K., Pekour, M., Fast, J., Xu, Q., Zhang, P., Yang, Q., Shaw, W. J., and Flaherty, J.: Evaluation of Single-Doppler Radar Wind Retrievals in Flat and Complex Terrain, *J. Appl. Meteor. Climatol.*, 53, 1920–1931, 2014.
- Nicol, J. C., Hogan, R. J., Stein, T. H. M., Hanley, K. E., Clark, P. A., Halliwell, C. E., Lean, H. W., and Plant, R. S.: Convective updraught evaluation in high-resolution NWP simulations using single-Doppler radar measurements, *Q.J.R. Meteorol. Soc.*, 141, 3177–3189, 2015.
- O’Brien, J. J.: Alternative Solutions to the Classical Vertical Velocity Problem, *J. Appl. Meteor.*, 9, 197–203, 1970.
- Ogura, Y. and Phillips, N. A.: Scale Analysis of Deep and Shallow Convection in the Atmosphere, *J. Atmos. Sci.*, 19, 173–179, 1962.
- Pauley, P. M. and Wu, X.: The Theoretical, Discrete, and Actual Response of the Barnes Objective Analysis Scheme for One- and Two-Dimensional Fields, *Mon. Wea. Rev.*, 118, 1145–1164, 1990.
- Potvin, C. K. and Wicker, L. J.: Comparison between Dual-Doppler and EnKF Storm-Scale Wind Analyses: Observing System Simulation Experiments with a Supercell Thunderstorm, *Mon. Wea. Rev.*, 140, 3972–3991, 2012.
- Potvin, C. K., Betten, D., Wicker, L. J., Elmore, K. L., and Biggerstaff, M. I.: 3DVAR versus Traditional Dual-Doppler Wind Retrievals of a Simulated Supercell Thunderstorm, *Mon. Wea. Rev.*, 140, 3487–3494, 2012a.
- Potvin, C. K., Wicker, L. J., and Shapiro, A.: Assessing Errors in Variational Dual-Doppler Wind Syntheses of Supercell Thunderstorms Observed by Storm-Scale Mobile Radars, *J. Atmos. Oceanic Technol.*, 29, 1009–1025, 2012b.



- Protat, A. and Zawadzki, I.: A Variational Method for Real-Time Retrieval of Three-Dimensional Wind Field from Multiple-Doppler Bistatic Radar Network Data, *J. Atmos. Oceanic Technol.*, 16, 432–449, 1999.
- Ray, P. S., Ziegler, C. L., Bumgarner, W., and Serafin, R. J.: Single- and Multiple-Doppler Radar Observations of Tornadoic Storms, *Mon. Wea. Rev.*, 108, 1607–1625, 1980.
- 5 Ryzhkov, A. V., Giangrande, S. E., Melnikov, V. M., and Schuur, T. J.: Calibration Issues of Dual-Polarization Radar Measurements, *J. Atmos. Oceanic Technol.*, 22, 1138–1155, 2005.
- Shapiro, A., Potvin, C. K., and Gao, J.: Use of a Vertical Vorticity Equation in Variational Dual-Doppler Wind Analysis, *J. Atmos. Oceanic Technol.*, 26, 2089–2106, 2009.
- Shapiro, A., Willingham, K. M., and Potvin, C. K.: Spatially Variable Advection Correction of Radar Data. Part I: Theoretical Considerations,
 10 *J. Atmos. Sci.*, 67, 3445–3456, 2010.
- Testud, J. and Chong, M.: Three-Dimensional Wind Field Analysis from Dual-Doppler Radar Data. Part I: Filtering, Interpolating and Differentiating the Raw Data, *J. Climate Appl. Meteor.*, 22, 1204–1215, 1983.
- Trapp, R. J. and Doswell, C. A.: Radar Data Objective Analysis, *J. Atmos. Oceanic Technol.*, 17, 105–120, 2000.
- Tridon, F., Battaglia, A., Kollias, P., Luke, E., and Williams, C. R.: Signal Postprocessing and Reflectivity Calibration of the Atmospheric
 15 Radiation Measurement Program 915-MHz Wind Profilers, *Journal of Atmospheric and Oceanic Technology*, 30, 1038–1054, 2013.
- Williams, C. R.: Vertical Air Motion Retrieved from Dual-Frequency Profiler Observations, *J. Atmos. Oceanic Technol.*, 29, 1471–1480, 2012.
- Wu, J., Del Genio, A. D., Yao, M.-S., and Wolf, A. B.: WRF and GISS SCM simulations of convective updraft properties during TWP-ICE, *J. Geophys. Res.*, 114, D04 206, 2009.

Table 1. Prominent convective events during MC3E, including a brief description and approximate time frame each event was sampled by UAZR-C1.

Event	Description	Time frame (UTC)
25 Apr 2011	Isolated, elevated convection	0900-1100
11 May 2011*	Isolated convection, widespread stratiform precipitation	1800-2300
20 May 2011 [†]	Mesoscale convective system, squall line	0600-1600
23 May 2011 [†]	Isolated, severe convection	2130-2300
24 May 2011 [†]	Isolated, severe convection	2100-2230

* CSAPR-I7 nonoperational

[†] XSAPR-I6 data recording issue



Table 2. Operational parameters of the ARM XSAPR, CSAPR, and UAZR during MC3E (convection mode).

Parameter	XSAPR	CSAPR	UAZR (long mode)
Frequency (GHz)	9.4	6.3	0.915
Wavelength (cm)	3.2	5.4	33.0
PRF (kHz)	2.2	1.2	8.3
Pulse width (ns)	460	800	2833
Nyquist velocity (m s^{-1})	16.8	16.5	20.0
3-dB beamwidth (deg)	1.2	1.0	9.0
Range resolution (m)	50	120	200*
Temporal resolution (s)	360	420	6
Maximum range (km)	40	117	15
Number of elevations	22	17	–
Elevation range (deg)	0.5-50.1	0.8-42.0	–

* UAZR dataset has 120 m range resolution.

Table 3. Summary of 3DVAR constraint weights derived from sensitivity analysis. Study values indicate the weight values used in this study. Nominal values reflect those used in previous OSSE studies. Equation (1) produces Λ_o values between 0 and 1 for this study.

Weight	Analysis	Study	Nominal
Λ_o	–	(0, 1)	1
Λ_c	(250, 1000)	500	1
Λ_b	(0, 0.5)	0.01	0.01
Λ_p	–	1000	–
Λ_{su}	(0, 100)	1	1
Λ_{sv}	(0, 100)	1	1
Λ_{sw}	(0, 100)	0.1	0.1



Table 4. Radar reflectivity comparisons between CSAPR-I7 and UAZR-C1 at three characteristic heights for all events. Error statistics have units of dBZ.

Event	Height (km AGL)	Sample Size	MBE	MAE	RMSE	ρ	r
25 Apr 2011							
	2	28	-1.00	2.22	3.79	0.95	0.80
	6	23	-1.62	2.73	3.51	0.93	0.64
	8	24	-1.09	2.50	3.81	0.92	0.67
	All	864	-0.94	2.97	3.96	0.94	0.55
11 May 2011*							
	2	70	-2.11	2.45	3.57	0.86	0.47
	6	85	-2.04	2.23	2.98	0.62	0.44
	8	69	-0.41	1.62	2.11	0.87	0.38
	All	2462	-1.16	1.98	2.79	0.92	0.40
20 May 2011							
	2	52	-2.11	2.33	3.24	0.97	0.77
	6	68	-1.90	2.28	3.79	0.79	0.76
	8	54	-1.29	1.79	3.60	0.85	0.70
	All	1983	-1.66	2.32	3.71	0.90	0.62
23 May 2011							
	2	6	-1.10	3.29	3.68	0.73	0.53
	6	19	-3.86	4.02	4.83	0.86	0.59
	8	11	-0.94	1.97	2.34	0.73	0.39
	All	398	-1.75	3.18	4.03	0.82	0.34
24 May 2011							
	2	6	-0.98	2.45	3.03	0.66	0.48
	6	16	-1.51	3.41	4.85	0.90	0.69
	8	29	-1.31	3.77	4.45	0.72	0.58
	All	557	-0.93	3.50	4.58	0.86	0.44

* Comparison between KVNK and UAZR-C1.



Table 5. Vertical air motion comparisons between 3DVAR and UAZR-C1 at three characteristic heights for all events. Error statistics have units of m s^{-1} .

Event	Height (km AGL)	Sample					
		Size	MBE	MAE	RMSE	ρ	r
25 Apr 2011							
	2	20	-0.46	0.65	0.92	0.54	0.53
	6	20	1.18	1.58	1.86	0.43	0.51
	8	20	0.43	2.17	3.09	0.23	-0.03
	All	676	0.50	1.63	2.22	0.14	0.11
11 May 2011							
	2	27	0.02	0.79	1.05	0.34	0.35
	6	27	0.66	0.93	1.08	0.51	0.55
	8	27	0.23	0.61	0.74	0.68	0.63
	All	897	0.45	0.87	1.07	0.48	0.48
20 May 2011							
	2	55	0.38	0.99	1.24	0.22	0.69
	6	58	0.35	0.86	1.22	0.44	0.61
	8	51	0.14	0.94	1.49	0.38	0.15
	All	1871	0.29	0.92	1.27	0.32	0.50
23 May 2011							
	2	6	0.54	1.01	1.45	0.33	0.33
	6	19	0.42	0.99	2.31	0.32	0.41
	8	11	0.50	1.88	1.89	0.21	0.40
	All	398	0.52	1.74	2.11	0.29	0.40
24 May 2011							
	2	6	0.36	0.98	1.21	0.34	0.31
	6	16	0.39	1.32	1.75	0.51	0.29
	8	29	0.49	1.87	2.02	0.42	0.35
	All	557	0.50	1.41	2.01	0.49	0.47

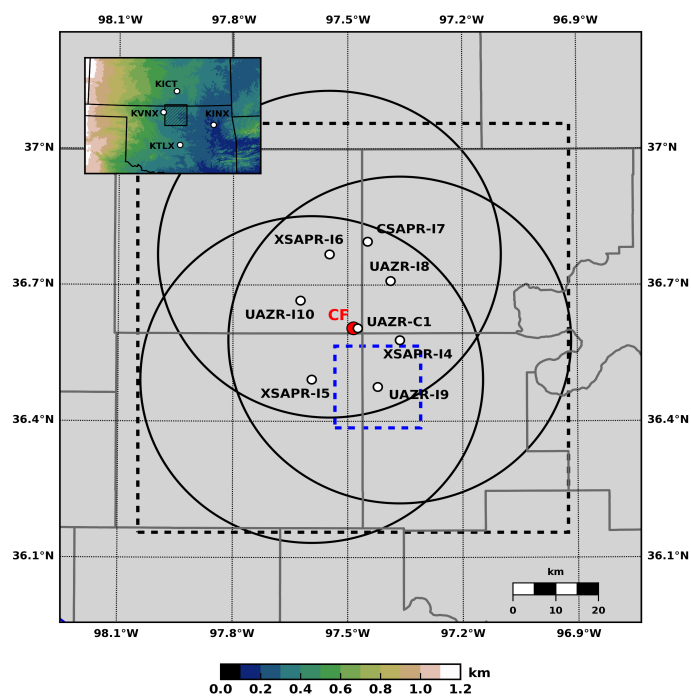


Figure 1. ARM SGP site with locations of scanning and profiling radars surrounding the Central Facility (CF). Dashed black box in main panel corresponds to a 100 km x 100 km horizontal analysis domain (also shown in inset panel). Black circles are 40 km XSAPR maximum range (see Table 2). The separate analysis domain used in the sensitivity analysis (see Section 4) is shown as the dashed blue box surrounding the southeast radar wind profiler (UAZR-I9). The inset panel provides the large-scale view of the region including surface elevation in kilometers above mean sea level and the closest NEXRAD WSR-88Ds.

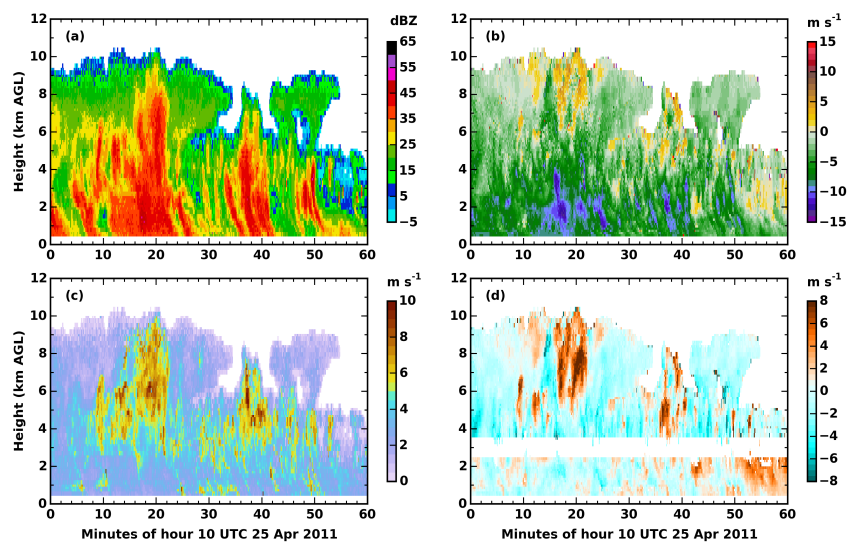


Figure 2. UAZR-C1 observations on 25 Apr 2011 (a) reflectivity (b) Doppler velocity (c) spectrum width and (d) corresponding vertical air motion retrieval. Within the melting layer (2.5-3.5 km AGL) no vertical air motion retrieval was attempted.

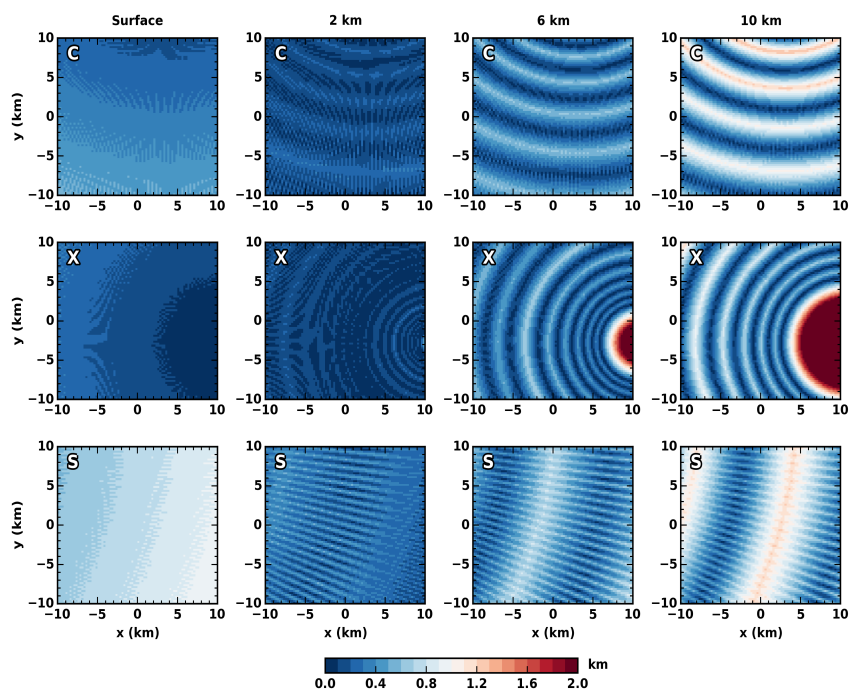


Figure 3. Nearest neighbour distances within 20 km x 20 km surrounding SGP CF for select radars CSAPR-I7 (C), XSAPR-I4 (X), and KVNK (S). Horizontal cross sections are at 0 km (surface), 2 km, 6 km, and 10 km AGL.

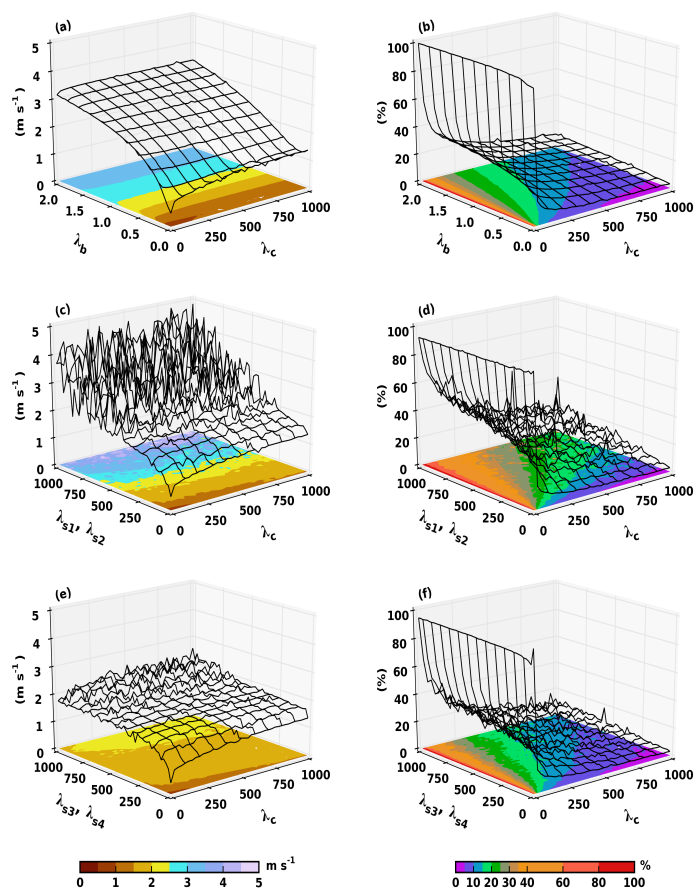


Figure 4. 3DVAR constraint weight sensitivity analysis for two metrics: CSAPR-I7 radial velocity RMSD (left column) and normalized mass continuity residual (right column). Sensitivity analysis is performed by perturbing (a-b) λ_c versus λ_b and (c-f) λ_c versus λ_{s2} , λ_{s3} , and λ_{s4} constraint weights. The nominal values for weights not being tested in a given panel are set to those used in previous OSSE studies (see Table 3).

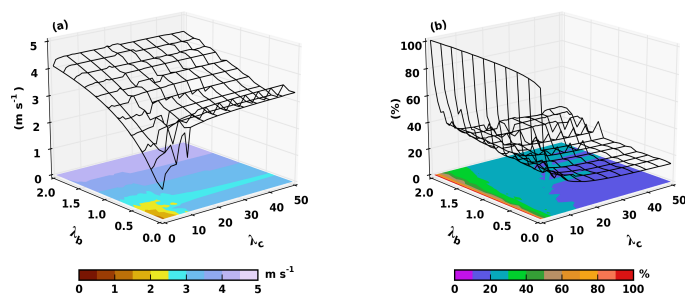


Figure 5. Similar to Fig. 4a-b but for an iterative upwards integration technique.

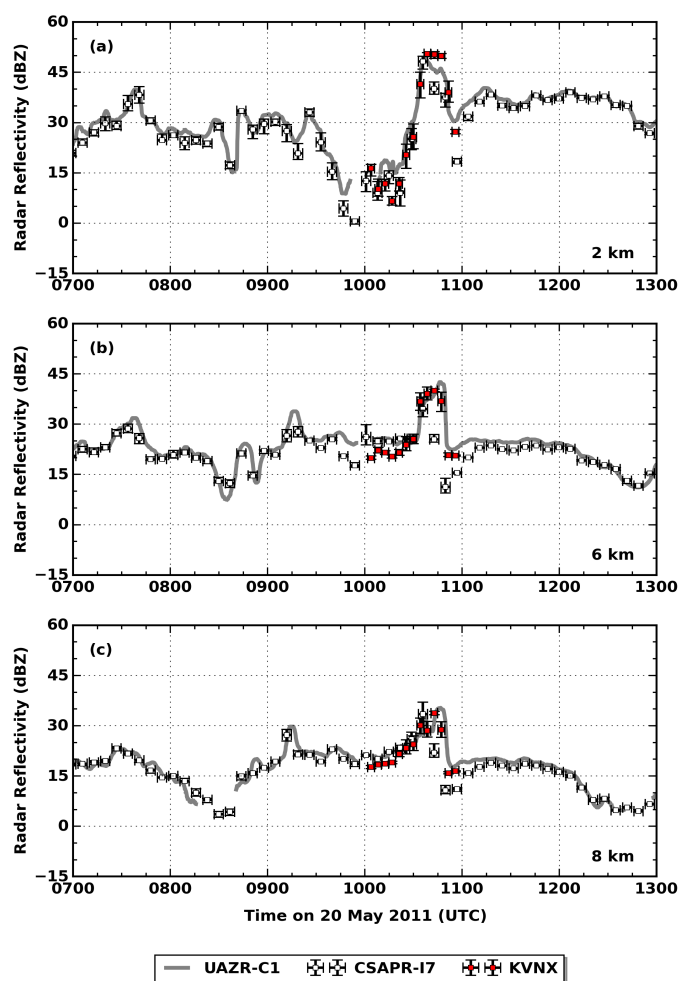


Figure 6. Radar reflectivity observations on 20 May 2011 at three characteristic heights (a) 2 km (b) 6 km and (c) 8 km AGL. CSAPR-17 and KVNx error bars indicate the full range of radar reflectivities within R_s and the volume scan time (valid time). UAZR-C1 observations have been filtered using a 61 x 7 time-height median filter. KVNx observations are shown between 1000-1100 UTC, exclusively.

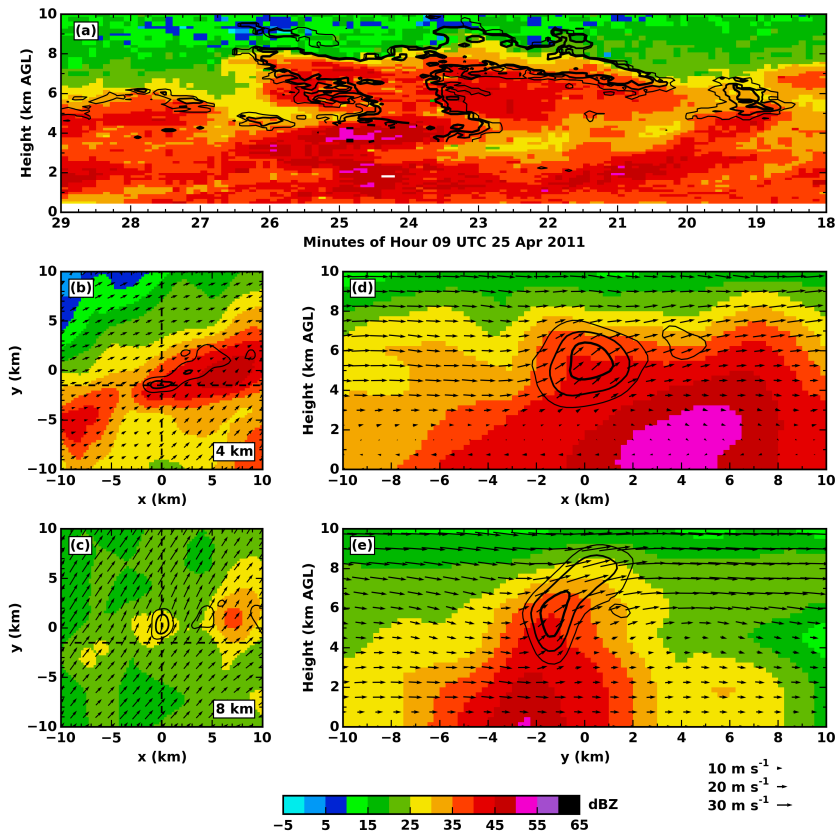


Figure 7. Two independent vertical air motion retrievals on 25 Apr 2011 from (a) 915-MHz radar wind profiler (UAZR-C1) and (b-e) 3DVAR. Radar reflectivity background and vertical velocity contours of 4 (light), 6 (medium), and 8 (thick) m s^{-1} are shown in all panels. Wind vectors are shown in every 3DVAR panel. The horizontal cross sections shown in (b-c) are at 4 and 8 km AGL, respectively, with dashed black lines indicating the corresponding vertical cross sections in (d-e). The 3DVAR retrieval was derived from scanning radar observations recorded between 0916-0924 UTC. The origin in (b-e) corresponds to the location of UAZR-C1.

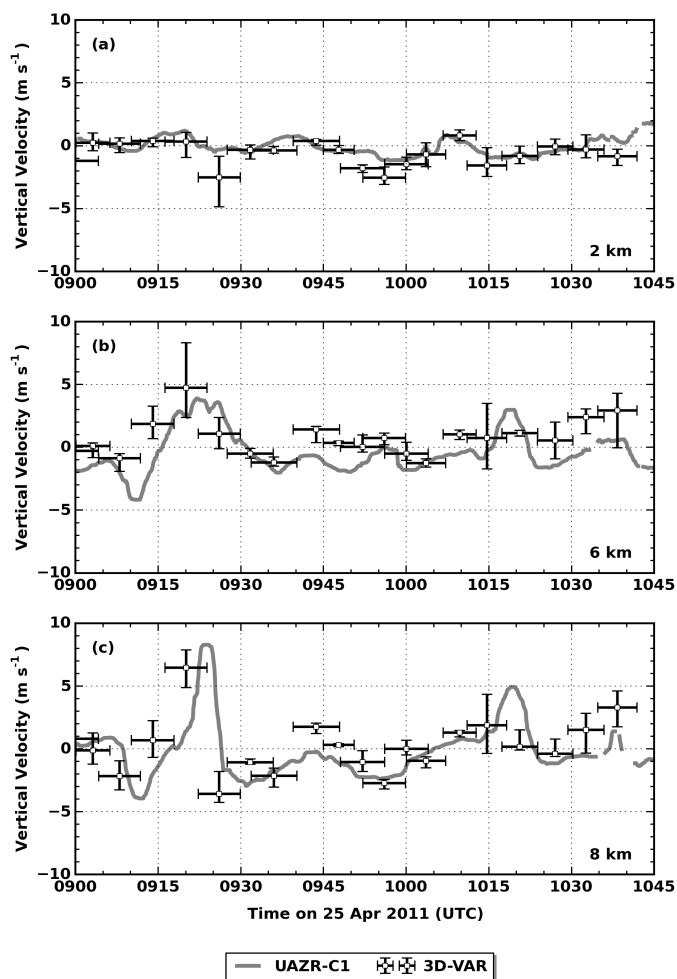


Figure 8. Vertical air motion time series on 25 Apr 2011 at three characteristic heights (a) 2 km (b) 6 km and (c) 8 km AGL. 3DVAR error bars indicate the full range of vertical velocities within R_s and the 3DVAR valid time. UAZR-C1 retrievals have been filtered using a 61 x 7 time-height median filter.

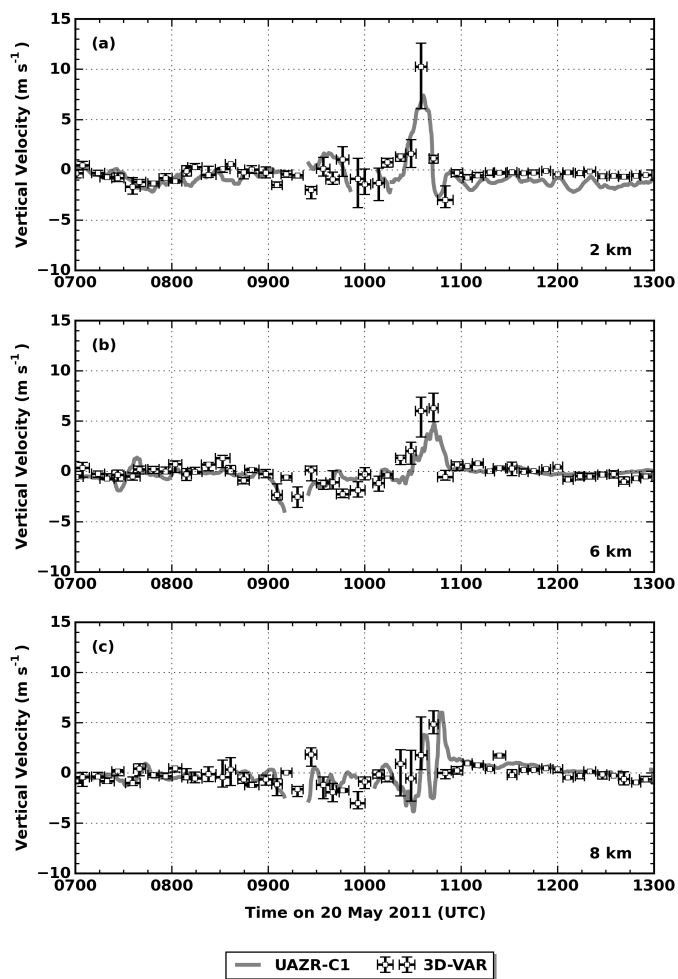


Figure 9. Similar to Fig. 8 but for 20 May 2011.

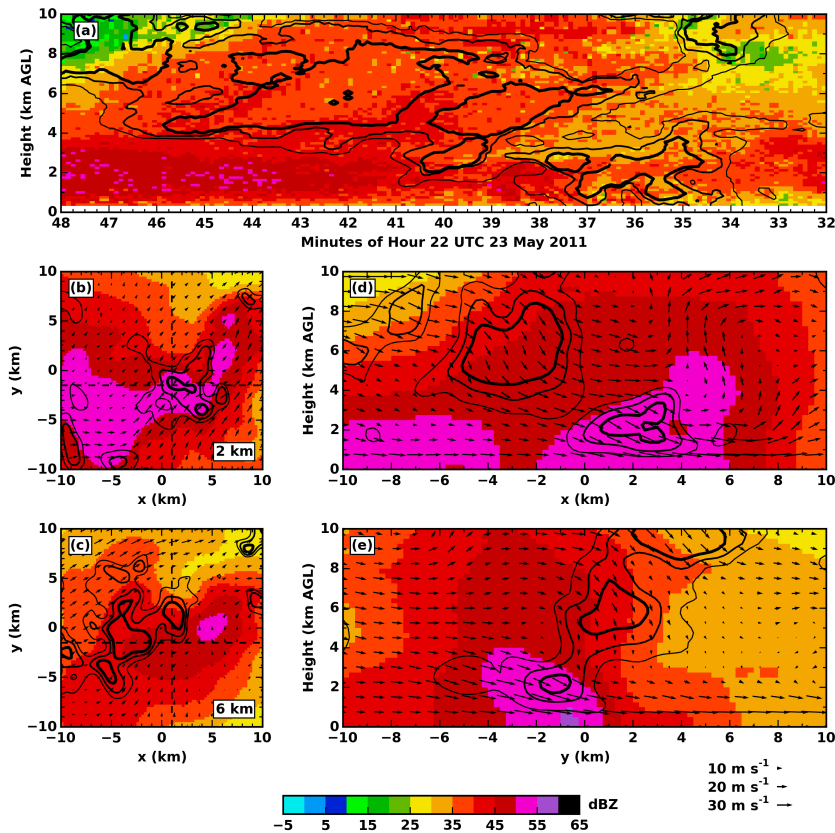


Figure 10. Two independent vertical air motion retrievals on 23 May 2011 from (a) 915-MHz radar wind profiler (UAZR-I9) and (b-e) 3DVAR. Radar reflectivity background and vertical velocity contours of -4 (light), -6 (medium), and -8 (thick) m s^{-1} are shown in all panels. Wind vectors are shown in all 3DVAR panels. Horizontal cross sections shown in (b-c) are at 2 and 6 km AGL, respectively, with dashed black lines indicating the corresponding vertical cross sections in (d-e). The 3DVAR retrieval was derived from scanning radar observations recorded between 2236-2243 UTC. The origin in (b-e) corresponds to the location of UAZR-I9.

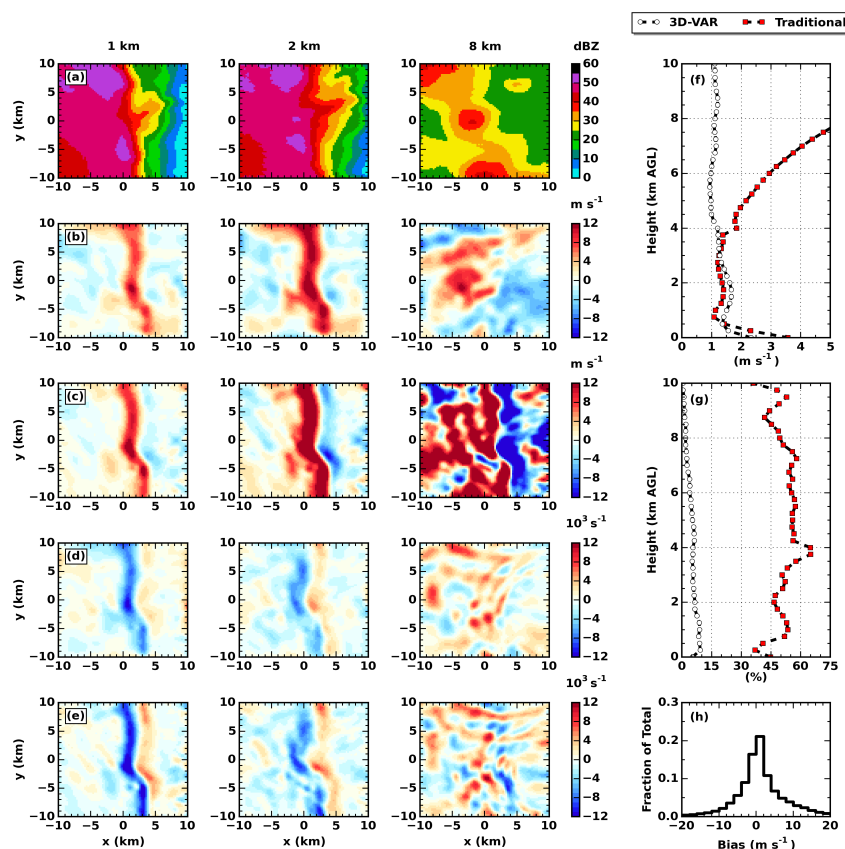


Figure 11. Comparison of 20 May 2011 squall line wind retrieval between 3DVAR and iterative upwards integration technique, showing (a) radar reflectivity (b-c) 3DVAR and iterative vertical air motion, respectively (d-e) 3DVAR and iterative horizontal wind divergence, respectively (f) CSAPR-I7 radial velocity RMSD profile (g) NMCR profile and (h) vertical air motion bias (3DVAR minus iterative; 2 m s^{-1} bin width). Select heights for (a-e) are 1 km, 2 km, and 8 km AGL. Origin in (a-e) corresponds to CF.